# Experimental realization of topologically protected unidirectional surface magnon polaritons on ceramic YIG ferrites

Alexander M. Holmes ,\* Mohsen Sabbaghi, and George W. Hanson University of Wisconsin-Milwaukee, Milwaukee, Wisconsin 53211, USA

(Received 18 June 2021; revised 9 December 2021; accepted 10 December 2021; published 28 December 2021)

Topologically protected, unidirectional surface magnon polaritons (SMPs) guided along the interface between air and ferrimagnetic yttrium iron garnet slab structures, biased with an external static magnetic field in the Voigt configuration, are realized experimentally by measuring the S-parameters between two small loop magnetic dipole antennas that launch and receive the SMP. Transmission is compared in the two cases where an abrupt change in the form of a step is present and absent in the interface. We find that transmission of the SMP peaks near the same level in each case, a sign of its topological protection. In addition, the dependence of isolation on slab thickness is investigated for a specified antenna configuration.

DOI: 10.1103/PhysRevB.104.214433

#### I. INTRODUCTION

Recently, a connection to momentum space topology has been made for plasmonic and ferrimagnetic continua biased with an external static magnetic field in the Voigt configuration [1-9], where bulk electromagnetic waves propagate in a direction perpendicular to the bias; see [10-14] for comprehensive reviews. In this configuration, the field profile (i.e., polarization) of the wave may be decomposed into transverse-magnetic (TM) and -electric (TE) bulk modes, where transverse is defined with respect to the propagation direction. When the external bias is removed, these modes have the same dispersion (i.e., their wave numbers are degenerate). However, once the bias is applied, the degeneracy is lifted, and a nontrivial band gap forms in the TM/TE dispersion associated with plasmonic/ferrimagnetic continua over a frequency range wherein the effective permittivity/permeability experienced by the mode is negative. The nontrivial nature of the band gap stems from the fact that time-reversal (TR) symmetry in the material response is broken due to the applied bias, which results in a nonzero Berry curvature, described as a rotation in momentum space of the Berry connection, defined in terms of the material response tensor and TM/TE polarization [1,2].

From a topological perspective, a band gap in the dispersion of bulk modes is characterized by a topological invariant (usually normalized to be integer-valued) called the gap Chern number  $C_{\text{gap}}$  defined in terms of the Berry curvature associated with modes that propagate below the band gap [12]. The band gap is classified as topologically trivial when  $C_{\text{gap}} = 0$ (a trivial gap Chern number may also indicate the absence of a band gap in the dispersion) and nontrivial when  $C_{\text{gap}} \neq 0$ . For biased plasmonic/ferrimagnetic continua, it has been shown

that the TM/TE gap Chern number is +1 [1,15], therefore classifying the band gap as nontrivial. Moreover, when interfaced with another material for which the bulk dispersion is topologically trivial, the difference between gap Chern numbers associated with each material,  $\Delta C_{\text{gap}} = 1 - 0 = 1$ , corresponds to the number of unidirectional surface wave modes that propagate in the nontrivial bulk band gap. The correspondence between bulk and surface wave modes made via the gap Chern number, known as the bulk-edge correspondence principle, has been studied extensively for periodic photonic structures [16-21], and recently, the concept has been extended to continuous media [22–24].

The unidirectional nature of the surface wave modes grants them topological protection against reflection when encountering an abrupt change (e.g., a step) in the material interface [25–27]. And, because these modes propagate in the nontrivial bulk band gap, they are immune to diffraction into the bulk. However, diffraction into the bulk of the interfaced trivial medium is possible if it lacks a common band gap (e.g., air) [28]. While the aforementioned description in terms of momentum space topology is not really needed (i.e., classical terms concerning nonreciprocity and band gaps already describe the phenomena [10,29]), the language of topology provides new insights into the underlying physics and allows, for instance, the potential engineering of photonic structures to achieve nontrivial gap Chern numbers [17], which could be quite useful in designing nonreciprocal devices such as isolators [30–33], gyrators [34], circulators [35], and directional couplers [15,36].

Although the existence of topologically protected surface wave modes supported by periodic photonic structures has been experimentally verified [37-41], here we verify, for the first time, the existence of a topologically protected surface magnon polariton (SMP) mode (i.e., a type of surface wave mode that arises from the coupling between the electromagnetic-field and magnetic dipole polarization of a material) guided along the interface between a biased ferrimagnetic yttrium iron garnet (YIG) continuum and

<sup>\*</sup>holmesam@uwm.edu

<sup>†</sup>sabbagh2@uwm.edu

<sup>‡</sup>george@uwm.edu

air. To demonstrate topological protection, we measure the S-parameters between two small loop magnetic dipole antennas that launch and receive the SMP and show that transmission of the SMP remains largely unaffected when an abrupt change in the form of a step is present in the interface.

In Sec. II, we provide a brief review of the theory already well established by the community that describes the topologically protected SMP and provide numerical and simulated results that give qualitative and quantitative insight into the propagation characteristics. In Sec. III, we provide an extensive overview of the experimental apparatus and a detailed analysis of the measurements.

### II. THEORY AND SIMULATION

In this section, we provide a brief review of the theory necessary to predict the existence of a topologically protected SMP mode guided along the interface between YIG, biased with an external magnetic field in the Voigt configuration, and air. The material response, dispersion of guided electromagnetic modes, excitation method, and the effects of nonuniformity in the external bias distribution are discussed in detail.

# A. Material response

Magnetic anisotropy in the material response of ceramic YIG ferrites is achieved by applying an external static (DC) magnetic bias field  $\mathbf{H}_0$  which induces a DC magnetization  $\mathbf{M}_0$  parallel to the bias. As a general consideration, the internal field of the YIG is reduced from the external field by a demagnetizing term that depends on the geometry and bias configuration. However, in the following analysis, we consider a thin square plate magnetized in the Voigt configuration [42] for which the demagnetizing term may be neglected [43]. The details of this contribution and its potential effect on the response are therefore omitted for conciseness.

Working in the saturated regime of the YIG hysteresis curve, we consider biases that are well beyond the coercive field, which may be anywhere from 1 to a few Oe (i.e.,  $\sim 10$  to  $\sim 50$  mT). In this regime, the DC magnetization is maximized to the point of saturation  $\mathbf{M}_s$ , and small signal analysis may be used to linearize Maxwell's equations governing electromagnetic wave propagation. The linear relationship between a time harmonic (AC) magnetic-field  $\mathbf{H}$  and resultant AC magnetization  $\mathbf{M}$  such that  $|\mathbf{H}| \ll |\mathbf{H}_0|$  is given by  $\mathbf{H} + \mathbf{M} = \bar{\mu} \cdot \mathbf{H}$ , where

$$\bar{\mu} = \mu_{\perp}(\bar{\mathbf{I}} - \hat{\mathbf{H}}_0 \hat{\mathbf{H}}_0) - j\mu_{\times}(\hat{\mathbf{H}}_0 \times \bar{\mathbf{I}}) + \mu_{\parallel} \hat{\mathbf{H}}_0 \hat{\mathbf{H}}_0 \tag{1}$$

is the relative permeability tensor derived semiclassically from the Landau-Lifshitz-Gilbert equation [44] describing precessional motion of the total magnetization vector  $\mathbf{M}_s + \mathbf{M}$ . The dispersive tensor elements with respect to the radial frequency  $\omega = 2\pi f$  are given by

$$\mu_{\perp} = 1 + \frac{\omega_s \tilde{\omega}_0}{\tilde{\omega}_0^2 - \omega^2}, \quad \mu_{\times} = \frac{\omega_s \omega}{\tilde{\omega}_0^2 - \omega^2}, \quad \mu_{\parallel} = 1, \quad (2)$$

where  $\omega_s = \mu_0 \gamma M_s$  and  $\tilde{\omega}_0 = \omega_0 + j\alpha\omega$  with  $\omega_0 = \mu_0 \gamma H_0$ ; the quantities  $\mu_0$ ,  $\omega_0$ , and  $\gamma = g_{\rm eff} \mu_{\rm B}/\hbar$  are, respectively, the permeability of free space, Larmor precessional (resonant)

TABLE I. YIG response parameters.

Saturation magnetization	$\mu_0 M_s$	$1820 \pm 20\% \text{ [Gs]}$
Effective Landé g factor	$g_{ m eff}$	2.02
Resonance linewidth	$\Delta H$	18 + 20% [Oe]
Effective linewidth	$\Delta H_{ m eff}$	3 [Oe]
Relative permittivity	arepsilon	$15 \pm 5\%$
Dielectric loss tangent	$tg\delta$	0.0002
Linewidth frequency	$f_0^*$	9.3 [GHz]

frequency, and gyromagnetic ratio defined in terms of the effective Landé g-factor  $g_{\rm eff}$ , Bohr magneton  $\mu_{\rm B}$ , and reduced Planck constant  $\hbar$ . Material losses are accounted for in the loss rate  $\alpha$  which is well defined on and off resonance at saturation [45].

Resonant cavity methods make it possible to determine  $\alpha$  by measuring the linewidth  $\Delta H$  associated with the imaginary part of  $\mu_{\perp}$  at resonance [46]. In the saturated regime,  $\alpha = \mu_0 \gamma \, \Delta H / 4\pi \, f_0^*$ , where  $f_0^*$  denotes the resonant frequency at which the linewidth is measured. Off resonance, losses decrease significantly and the replacement of  $\Delta H$  with  $\Delta H_{\rm eff}$  in the calculation of  $\alpha$  is made.

Table I provides the necessary parameters used to calculate the relative permeability tensor elements of the YIG obtained from the specification sheet provided by the manufacturer, Exxelia Temex. In addition to those already mentioned, the table lists the relative dielectric constant  $\varepsilon$  and loss tangent  $tg\delta$ .

### B. Dispersion of guided electromagnetic modes

To obtain the dispersion of guided electromagnetic modes supported by a YIG slab of thickness 2h, biased with a static uniform magnetic-field  $\mathbf{H}_0 = \mathbf{\hat{z}}H_0$  in the Voigt configuration and interfaced with air, we treat the slab as invariant with respect to the x-z plane and assume the propagation direction is perpendicular to the bias (i.e., the wave-vector  $\mathbf{k}$  is perpendicular to  $\mathbf{H}_0$ ), in which case the wave may be decomposed into TE and TM modes, where transverse is defined with respect to  $\mathbf{k}$ . In the air and YIG regions, the electric  $E_z^{\text{TE}}$  and magnetic  $H_z^{\text{TM}}$  vector components of TE and TM bulk modes satisfy the source-free scalar Helmholtz equation,

$$(\partial_y^2 - q_x^2 + [k_{\text{TE}}^2, k_{\text{TM}}^2])[E_z^{\text{TE}}, H_z^{\text{TM}}] = 0,$$
 (3)

where the bulk wave-numbers  $k_{\rm TE}=k_{\rm TM}=k_0\sqrt{\varepsilon_{\rm T}\mu_{\rm T}}$  in air, and  $k_{\rm TE}=k_0\sqrt{\varepsilon\mu_{\rm eff}}$  and  $k_{\rm TM}=k_0\sqrt{\varepsilon\mu_{\rm H}}$  in YIG; parameters  $\varepsilon_{\rm r}$  and  $\mu_{\rm r}$  are the relative permittivity and permeability of air,  $\mu_{\rm eff}=\mu_{\perp}-\mu_{\times}^2/\mu_{\perp}$  is the effective relative permeability experienced by the TE modes in YIG, and  $k_0$  is the free space wave number (all other parameters are defined in Sec. II A). The magnetic  $(H_x^{\rm TE},H_y^{\rm TE})$  and electric  $(E_x^{\rm TM},E_y^{\rm TM})$  vector components of TE and TM bulk modes are then recoverable from Maxwell's equations on solving Eq. (3) for  $E_z^{\rm TE}$  and  $H_z^{\rm TM}$ .

Of particular interest are the topologically nontrivial TE bulk modes of YIG which experience an effective permeability  $\mu_{\text{eff}}$  dependent on the external magnetic bias. Over the frequency range  $\omega \in [\omega_l, \omega_u]$ , where  $\omega_u = \omega_0 + \omega_s$  and  $\omega_l = \sqrt{\omega_0 \omega_u}$ , the response may be characterized as an imperfect

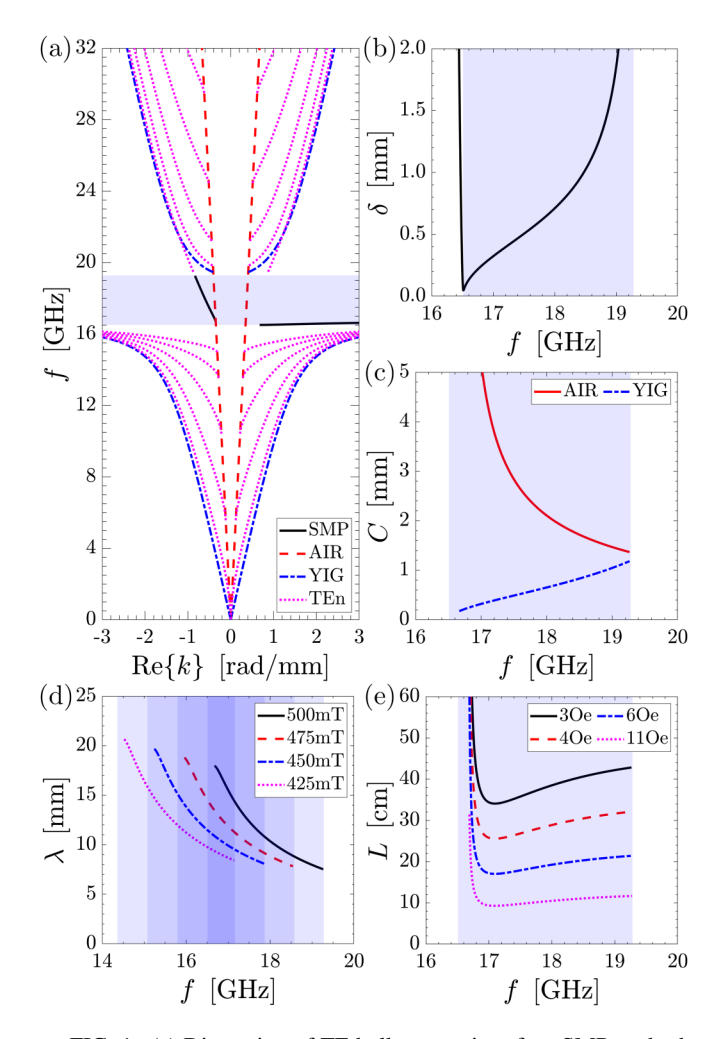


FIG. 1. (a) Dispersion of TE bulk, upper interface SMP, and nth order guided modes ( $n \in \{0, 1, 2, 3, 4\}$ ) for a 6-mm thick YIG slab (i.e., h = 3 mm) biased with 500 mT in the Voigt configuration and interfaced with air. The shaded frequency band highlights the TE bulk band gap. (b) Skin depth of YIG in the band gap. (c) Confinement of the SMP in the air and YIG regions. (d) SMP wavelength for magnetic bias settings that decrease in magnitude from 500 mT in steps of 25 mT. The shaded band-gap regions correspond to each bias setting with maximum overlap occurring over a narrow frequency band centered about  $\sim$ 16.8 GHz. (e) Propagation length L of the SMP shown to decrease with increasing loss rate  $\alpha$  (i.e., increasing effective linewidth  $\Delta H_{\rm eff}$ ).

magnetic conductor with  $\text{Re}\{\mu_{\text{eff}}\} < 0$ , which corresponds to the nontrivial band gap that forms in the dispersion. As a result, the YIG has a finite skin depth  $\delta = 1/\text{Im}\{k_{\text{YIG}}\}$  in the band gap, where  $k_{\text{YIG}}$  denotes the TE bulk wave number in YIG (in the following,  $k_{\text{AIR}}$  likewise denotes the TE bulk wave number in air). Figure 1(b) shows how the skin depth varies in the band gap associated with a 500 mT bias. At the lower band-edge  $\omega_l$ , the YIG functions as a near perfect magnetic conductor with  $\delta \sim 0$  and gradually transitions back to an insulator as frequency increases, with  $\delta \to \infty$  as frequency approaches the upper band-edge  $\omega_u$ .

After obtaining the field profile of TE bulk modes in the air and YIG regions, the dispersion of TE guided modes supported by the slab (i.e., SMP and guided via total internal

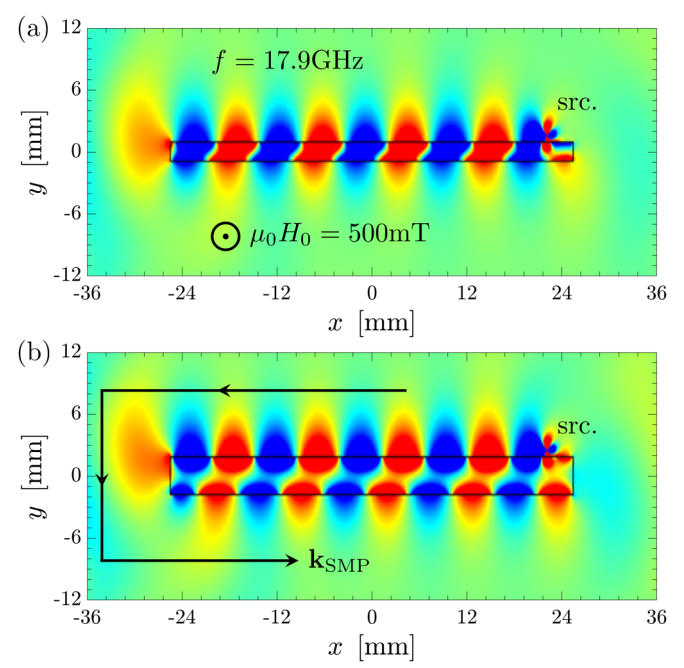


FIG. 2. FEM simulations performed in COMSOL of the SMP excitation using a near-field magnetic dipole point source (src.) oriented perpendicular to the upper interface and positioned near the right edge of each biased YIG slab having dimensions (a)  $50.6 \text{ mm} \times 1.8 \text{ mm}$  and (b)  $50.6 \text{ mm} \times 3.6 \text{ mm}$ . In each simulation, the computational domain is invariant with respect to the magnetic bias  $\mathbf{H}_0 = \mathbf{\hat{z}}H_0$  where  $\mu_0H_0 = 500 \text{ mT}$ , and the operating frequency is 17.9 GHz, corresponding to the band-gap center.

reflection) are obtained by enforcing continuity of  $E_z^{\rm TE}$  and  $H_x^{\rm TE}$  at each interface. It can be shown that the dispersion relation for TE modes guided by the slab via total internal reflection is [47,48]

$$q_x^2 \mu_r^2 \mu_x^2 / \mu_\perp^2 = [\kappa_{AIR} \mu_{eff} \coth(\kappa_{YIG} h) + \kappa_{YIG} \mu_r] \times [\kappa_{AIR} \mu_{eff} \tanh(\kappa_{YIG} h) + \kappa_{YIG} \mu_r], \quad (4)$$

where  $\kappa_{\nu}^2 = q_x^2 - k_{\nu}^2$  for  $\nu \in \{AIR, YIG\}$ . Cutoff frequencies for *n*th-order modes that propagate above/below the band gap are recovered when  $q_x = k_{AIR}$ ,

$$\omega_n^{\pm} = \sqrt{\frac{-B_n \pm \sqrt{B_n^2 - 4AC_n}}{2A}} : n \in \{0, 1, 2, \dots\},$$
 (5)

where

$$A = 4h^2(\varepsilon - \mu_{\rm r}\varepsilon_{\rm r}),\tag{6}$$

$$B_n = 4h^2 \left( \mu_r \varepsilon_r \omega_l^2 - \varepsilon \omega_u^2 \right) - n^2 \pi^2 c^2, \tag{7}$$

$$C_n = n^2 \pi^2 c^2 \omega_l^2. \tag{8}$$

In the thick slab limit  $h \to \infty$ , Eq. (4) factors into the dispersion relations of SMP modes that propagate in the band gap at the upper and lower interfaces of the slab [42,47],

$$0 = (\kappa_{\text{YIG}}\mu_{\text{r}} + \kappa_{\text{AIR}}\mu_{\text{eff}} - q_{x}\mu_{\text{r}}\mu_{\times}/\mu_{\perp})$$
$$\times (\kappa_{\text{YIG}}\mu_{\text{r}} + \kappa_{\text{AIR}}\mu_{\text{eff}} + q_{x}\mu_{\text{r}}\mu_{\times}/\mu_{\perp}). \tag{9}$$

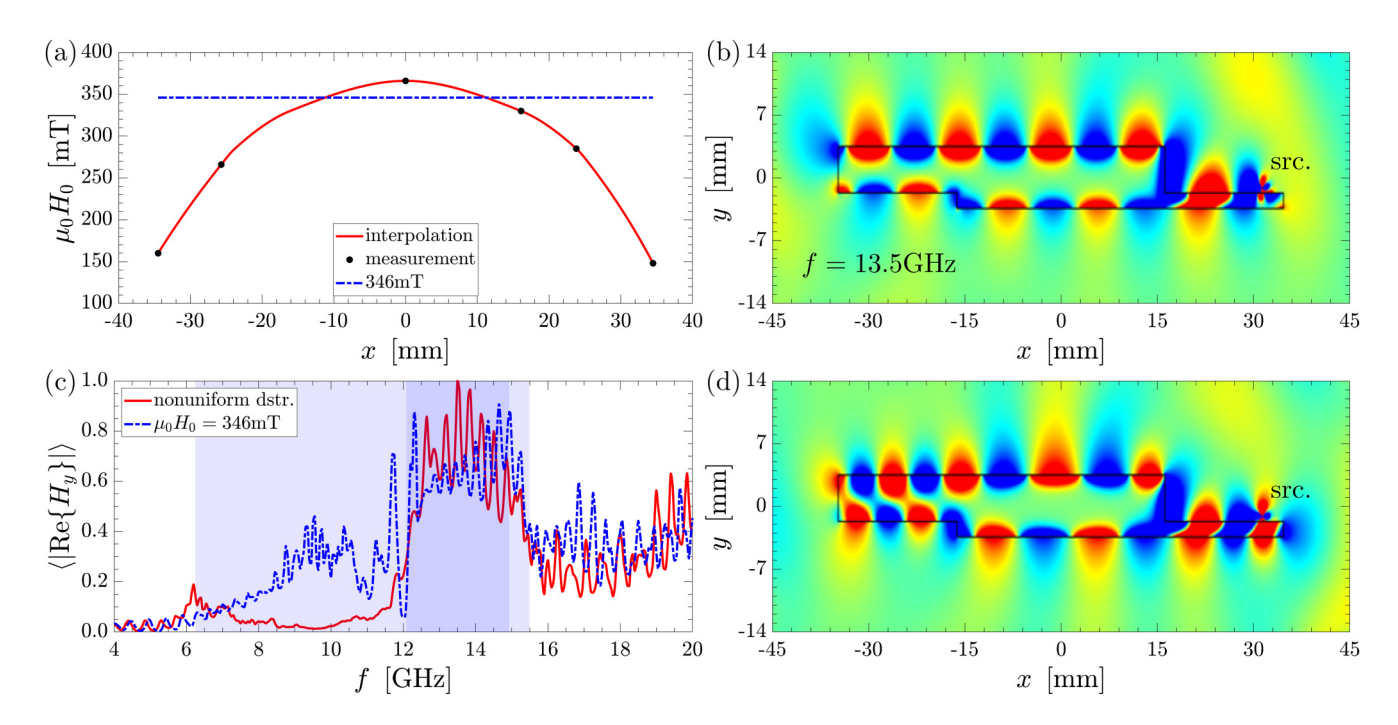


FIG. 3. (a) Uniform and nonuniform magnetic bias distributions considered in FEM simulations performed in COMSOL using a near-field magnetic dipole point source (src.) to generate the SMP field profiles on the YIG slab structure outlined in panels (b) and (d), respectively. (c) A spatial average of the magnetic-field magnitude normal to the uppermost interface, defined in Eq. (10) and normalized with respect to the maximum value associated with the nonuniform distribution. The dark shaded band centered about the selected operating frequency f = 13.5 GHz corresponds to the band-gap center associated with the uniform bias distribution, while the light shaded band corresponds to the broadened band gap associated with the nonuniform distribution. In each simulation, the computational domain is invariant with respect to the magnetic bias direction  $\hat{\mathbf{z}}$ .

Solutions for  $q_x$  that satisfy the  $n^{th}$  order guided [Eq. (4)] and SMP [Eq. (9)] mode dispersions are denoted  $k_{\text{SMP}}$  and  $k_{\text{TEn}}$ , respectively, and must be obtained via numerical root search since there exist no closed form solutions. While the dispersion of nth order guided modes is clearly reciprocal due to the  $q_x^2$  dependence, it can be shown that each SMP mode is unidirectional at the upper/lower interfaces of the slab, propagating in the  $\pm \hat{\mathbf{x}}$  direction for operating frequencies  $\omega \in [\omega_l, \omega_u - \omega_s/2, \omega_u]$ .

The dispersion of TE bulk, upper interface SMP, and nth order guided modes is shown in Fig. 1(a) for h = 3 mm and  $\mu_0 H_0 = 500$  mT. The SMP mode branch that propagates in the  $-\hat{\mathbf{x}}$  direction for  $\omega \in [\omega_u - \omega_s/2, \omega_u]$  attenuates differently on either side of the interface at rates  $\kappa_{AIR}$  and  $\kappa_{YIG}$  into the air and YIG regions. The higher these rates are the more tightly confined the SMP is to the interface. Confinement C = $1/\text{Re}\{\kappa\}$  of the SMP is shown in Fig. 1(c). At the lower bandedge  $\omega_u - \omega_s/2$ , the SMP is not well confined to the interface in the air region with  $C \to \infty$  but tightly confined in the YIG region with  $C \sim 0$ . As frequency increases, confinement increases/decreases in the YIG/air regions. In Fig. 1(d), the SMP wavelength  $\lambda = 2\pi/k_{\text{SMP}}$  is shown for a few bias settings that decrease in magnitude from 500 mT in steps of 25 mT. As bias decreases, the spectral location of the band-gap red shifts. Over a narrow band centered about ~16.8 GHz, the band gap is common to all magnetic biases, and for a set frequency, each SMP mode exists within it having wavelengths that decrease with bias. The figure also suggests that if a nonuniform bias, slowly varying with respect to the SMP wavelength, were distributed across the slab, the band gap would effectively

broaden (i.e., the transmission of bulk radiation between two points in the spatial plane would be blocked over a broader frequency range), with a strong SMP excitation likely possible at some operating frequency within the broadened band gap due to SMP mode overlap. In fact, simulation and experiment later confirm this theory. Figure 1(e) shows the profound effect that loss has on the propagation length  $L=1/[2\text{Im}\{k_{\text{SMP}}\}]$ . However, for this application, the band gap is far enough from the resonant frequency  $\omega_0$  (i.e., off resonance,  $\Delta H_{\text{eff}}=3\text{Oe}$  is used to define the loss rate  $\alpha$ ) and so loss does not significantly damp the SMP mode.

# C. SMP excitation

To excite the SMP mode, the easiest way is to use a nearfield source that induces a time harmonic magnetic dipole moment perpendicular to the air-YIG interface. For example, this type of excitation may be implemented experimentally using a small loop magnetic dipole antenna with the loop oriented in the plane of the interface. Figures 2(a) and 2(b) show field maps of the SMP excitation above 1.8- and 3.6mm thick YIG slabs using a magnetic dipole point source operating at the band-gap center frequency associated with a uniform 500 mT bias. To generate the field maps, finite element method (FEM) simulations are performed in COMSOL, where the computational domain in each case is invariant with respect to the bias direction 2. Due to a nonzero confinement  $C \sim 0.6$  mm in the YIG, as shown in Fig. 1(c), the magnetic-field components of the SMP normal to the upper and lower interfaces begin to interfere considerably as

thickness decreases from 3.6 mm, which forms a quasistanding wave within the slab.

#### D. Effects of nonuniformity

In Sec. IIB, we speculated from Fig. 1(d) that if a nonuniform bias, slowly varying with respect to the SMP wavelength, were distributed across the YIG between two points in the spatial plane, the band gap would effectively broaden since transmission of bulk radiation between the points would be blocked for operating frequencies within the broadened range. In addition, due to SMP mode overlap, we speculated that a strong SMP excitation would likely be possible for some operating frequency within the broadened band gap. In what follows, we provide a simulation that confirms this theory.

Drawing a connection between the simulation described here and the measurement described in Sec. III B, we consider the YIG slab structure shown in Figs. 3(b) and 3(d) which contains an abrupt change in the form of a step along the upper interface. The structure is biased with (b) a uniform 346mT, and (d) an interpolated nonuniform distribution obtained from measurement. The bias distributions in each case are shown in Fig. 3(a). In Fig. 3(c), a spatial average of the magnetic-field magnitude normal to the uppermost interface defined by

$$\langle |\text{Re}\{H_y\}| \rangle = \frac{1}{x_f - x_i} \int_{x_i}^{x_f} |\text{Re}\{H_y(x, y_0)\}| dx,$$
 (10)

with  $x_i = -34.5$  mm,  $x_f = 16.1$  mm, and  $y_0 = 3.6$  mm, is shown for the uniform and nonuniform bias distributions, where each quantity is normalized with respect to the maximum value associated with the nonuniform distribution. The averaged field provides qualitative insight into how intense the field is at the uppermost interface over a broad range of frequencies. For the uniform and nonuniform distributions, the field peaks as a result of SMP propagation at the center of the dark shaded frequency band, which corresponds to the band gap associated with the uniform distribution. Outside of this region where the SMP does not propagate, bulk radiation contributes to a nonzero field at the interface. However, for the nonuniform distribution, bulk radiation is suppressed significantly in the lightly shaded band corresponding to the broadened band gap relative to the case where the bias is uniform. Figures 3(b) and 3(d) show the SMP field profile for the uniform and nonuniform distributions, respectively, when the operating frequency is 13.5 GHz, corresponding to the band-gap center associated with the uniform bias. For the nonuniform distribution, SMP wavelength differs at various points along the interface in a way that is consistent with Fig. 1(d).

### III. EXPERIMENT

To demonstrate the effectiveness of topological protection, we designed an experiment to measure transmission of the SMP between two small loop magnetic dipole antennas displaced a short distance above the upper interface between air and various YIG slab structures, including those considered for simulation in Secs. II C and II D. Each structure is created by layering YIG plates having dimensions of 50.6 mm ×



FIG. 4. Top view of the apparatus used to conduct the experiment, where two neodymium ferromagnets in series bias a YIG slab in the Voigt configuration, and two small loop magnetic dipole antennas (labeled ant. 1,2) mounted onto 1.85-mm coaxial cables, displaced a small distance above the upper interface by an insulating cover (white), transmit and receive at operating frequencies between 4 and 22 GHz. The inset in the top right corner shows a zoomed view of the antennas formed by connecting the inner SMA conductor to the outer via a piece of 19 AWG copper wire with the enamel stripped off. A vector network analyzer (not shown) measures transmission.

 $50.6 \text{ mm} \times 1.8 \text{ mm}$ . Using a vector network analyzer, transmission is measured at operating frequencies in the range of 4 to 22 GHz.

A full top view of the apparatus used to conduct the experiment is shown in Fig. 4. Two  $2\text{in}^3$  neodymium magnets coated in nickel, manufactured by K&J Magnetics, are connected in series to provide a magnetic bias distribution across the thin edge of each structure. Individually, the magnets provide a maximum surface field of  $\sim 575$  mT. Additional perspective views of the apparatus are shown in Figs. 5(a), 5(c), and 6(a).

## A. Isolation dependence on slab thickness

For the system under study, signal isolation in the band gap is a measure of how efficiently the SMP is received by one antenna over the other. Since the SMP is unidirectional, an SMP launched by antenna 1 (ant. 1) takes the upper interface path, while an SMP launched by antenna 2 (ant. 2) takes the lower interface path. Due to the way the antennas are positioned, when the SMP is transmitted via the upper interface path, the flux is received more efficiently because there would be neither diffraction at the edges nor scattering at the antenna feeds before being received. However, for a thin slab such as the one shown in Fig. 2(a), a nonzero confinement may result in the magnetic field of an SMP taking the lower interface path being detected at the upper interface by the receive antenna

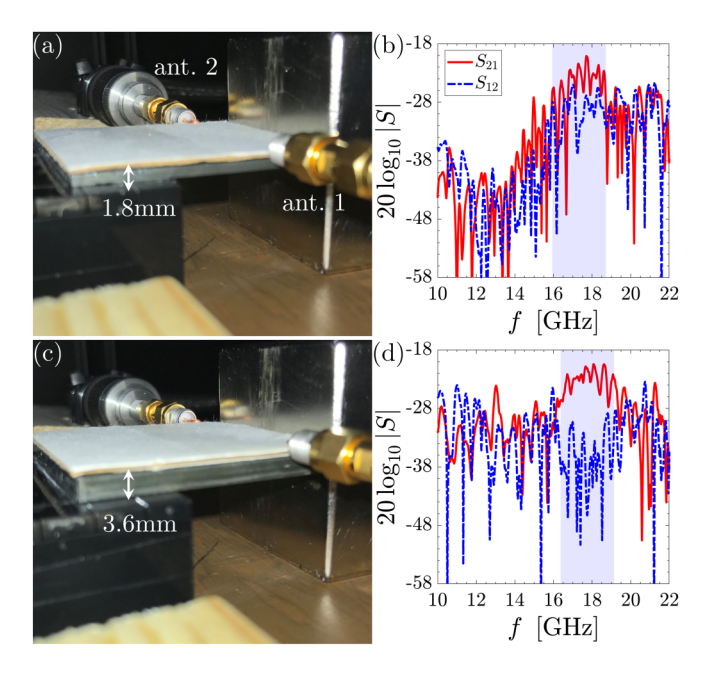


FIG. 5. (a), (c) Perspective views of the apparatus for single and double stacked YIG plates having a combined thickness of 1.8 and 3.6 mm. In each case, the  $\hat{\mathbf{z}}$  component of magnetic bias is measured using a gauss meter in the vicinity of 480 and 495 mT at a variety of points along the upper interface path between antennas. (b), (d) Measured transmission spectra for the 1.8- and 3.6-mm thick slabs, respectively. Transmission is nonreciprocal and peaks as a result of SMP propagation in the expected band-gap region associated with the measured bias.

(i.e., ant. 1). In this case, path preference becomes less clear and would result in low isolation.

Figures 5(a) and 5(c) show a perspective view of the apparatus for 1.8- and 3.6-mm thick slabs constructed from one and two-layered YIG plates. Using a MF100 Gauss meter by Extech Instruments, the  $\hat{\mathbf{z}}$  component of magnetic bias (i.e., the bias component perpendicular to the line of sight between antennas) is measured in the vicinity of (a) 480 mT and (b) 495 mT, with slight deviations from these values at various points along the upper interface path. In Figs. 5(b) and 5(d), the corresponding measured S-parameters are shown. Transmission of the SMP is nonreciprocal (i.e.,  $S_{21} \neq S_{12}$ ) with  $S_{21}$  peaking well within the expected band-gap region (shaded) associated with the measured bias. For this antenna configuration, we find a substantial increase in isolation when the slab thickness increases from 1.8 to 3.6 mm.

# **B.** Topological protection

The third slab structure under consideration is one having a step in the upper interface path comparable to one SMP wavelength. Layering four YIG plates, the structure shown in Figs. 3(b) and 3(d) is created by sliding the bottom plate out by 18.4 mm. This places its maximum dimension at 69 mm, slightly larger than the magnet dimension. As a result, the bias is substantially nonuniform across the structure relative to the previous two cases considered, but does not vary too significantly so as to dramatically alter the underlying physics. Figure 6(a) shows a perspective view of the apparatus, with

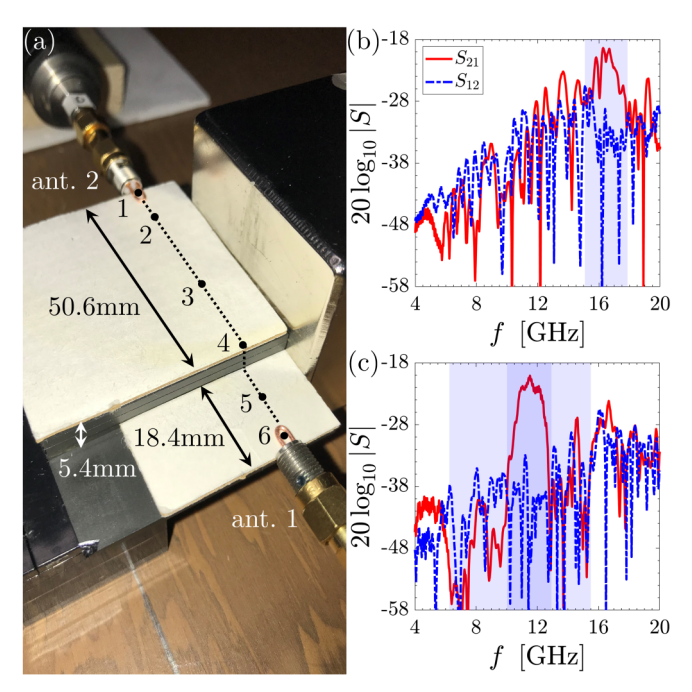


FIG. 6. (a) Perspective view of the apparatus for the YIG slab structure shown in Figs. 3(b) and 3(d), formed by stacking four YIG plates and sliding the bottom plate out 18.4 mm. The entire structure is centered on the magnet which results in a near symmetric nonuniform bias distribution across the structure [see Fig. 3(a) for the interpolated distribution]. Points labeled {1, 2, 3, 4, 5, 6} correspond to locations along the upper interface where the magnetic field is measured in the vicinity of {160, 266, 366, 330, 285, 148} mT. The distance of each point from point 1 are {8.8, 34.5, 50.6, 58.3, 69} mm. (b) Measured Sparameters for a three-layered structure, similar to those shown in Figs. 5(a) and 5(c), with the bias measured in the vicinity of 450 mT. (c) Measured S-parameters for the slab structure shown in (a). In (b), the shaded frequency band corresponds to the band gap associated with the measured bias. In (c), the lightly shaded band corresponds to the broadened bulk band gap associated with the nonuniform bias distribution, and the dark shaded band centered about peak  $S_{21}$ corresponds to the band gap associated with a uniform 275 mT bias.

the structure centered on the magnet. Points  $\{1, 2, 3, 4, 5, 6\}$  correspond to locations along the upper interface path where the  $\hat{\mathbf{z}}$  component of the bias is measured. The measured values and relative distances from point 1 are provided in the figure caption and shown in Fig. 3(a).

Figures 6(b) and 6(c) show the measured transmission for a three-layer slab, similar to the one and two layer slabs shown in Figs. 5(a) and 5(c) with the  $\hat{\mathbf{z}}$  component of the bias measured in the vicinity of 450 mT, and the elongated four-layered structure biased with a nonuniform field distribution. In Fig. 6(b), the shaded frequency band corresponds to the band gap associated with the measured bias, and in Fig. 6(c), the lightly shaded band corresponds to the broadened band gap associated with the nonuniform bias distribution, while the dark shaded band centered about peak  $S_{21}$  has the same bandwidth and location as the band gap associated with a uniform 275 mT bias. In all of the four cases considered, SMP transmission peaks in the band gap near the same level (i.e.,  $20 \log_{10} |S_{21}| \simeq -20 \text{dB}$ ), demonstrating that the SMP is

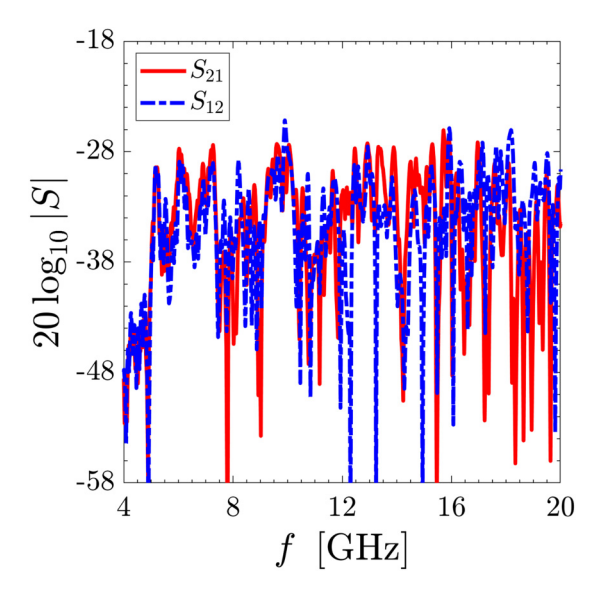


FIG. 7. Measured S-parameters for the slab structure shown in Fig. 6(a) when the bias is removed, where slight deviations in  $S_{21}$  and  $S_{12}$  are attributed to a small remnant magnetization. At operating frequencies beyond  $\sim$ 5 GHz, a fair amount of transmission occurs due to bulk radiation that is guided by the structure via total internal reflection. When biased, transmission is suppressed significantly in the broadened band gap as shown in Fig. 6(c).

indeed topologically protected against reflection. For reference, a transmission measurement obtained in the absence of bias (i.e., with the magnet removed) for the four-layered structure is shown in Fig. 7.

A peak in  $S_{21}$  is directly correlated with a peak in the magnetic flux associated with the SMP received by antenna 2. Likewise, the received flux may be correlated with a spatial average of the magnetic-field magnitude normal to and distributed across the uppermost interface. In Fig. 3(c), it is shown that this spatial average obtained from simulation peaks within the broadened band gap over a frequency band corresponding to the band gap associated with a uniform 346 mT bias and confirmed this peak was in fact due to SMP propagation by examining the field profile shown in Fig. 3(d).

However, in experiment, we find that  $S_{21}$  peaks within a frequency band corresponding to the band gap associated with a uniform 275 mT bias. The slight spectral shift of the SMP resonance observed in experiment is likely attributed to demagnetization (which we did not account for in our model), since the total bias field  $\mathbf{H}_0$  is not strictly oriented in the Voigt configuration (i.e., in the simulation, we only consider the bias component perpendicular to the line of sight between antennas). In addition, the broadened band gap effectively blocks transmission of bulk mode radiation between two points in the spatial plane which is evident from both simulation and experiment.

#### IV. CONCLUSION

In this work, we obtain experimental evidence of topologically protected unidirectional SMPs guided along the interface between air and various YIG slab structures biased with an external magnetic bias field in the Voigt configuration. The SMPs are transmitted and received via two small loop magnetic dipole antennas placed a distance across from each other near the interface. We show that for a fixed antenna position, isolation in the band gap increases with thickness as a result of the lower interface path becoming less preferred than the upper interface path. In addition, we show that the SMP is topologically protected against reflection when encountering an abrupt change in the interface as peak transmission of the SMP remains largely unaffected. Furthermore, we show in simulation and experiment that a fair degree of nonuniformity in the bias distributed across the structure has the net effect of broadening the bulk band gap without compromising the SMP resonance.

# ACKNOWLEDGMENTS

The authors thank Samaneh Pakniyat and Ali Hassani Gangaraj for helpful discussions pertaining to COMSOL simulations and Swadesh Poddar for his training on the vector network analyzer. Funding for this research was provided by the National Science Foundation under Grant No. EFMA-1741673.

<sup>[1]</sup> M. G. Silveirinha, Chern invariants for continuous media, Phys. Rev. B **92**, 125153 (2015).

<sup>[2]</sup> S. A. Hassani Gangaraj, M. G. Silveirinha, and G. W. Hanson, Berry phase, berry connection, and chern number for a continuum bianisotropic material from a classical electromagnetics perspective, IEEE J. Multiscale Multiphys. Comput. Techn. 2, 3 (2017).

<sup>[3]</sup> S. H. Gangaraj, A. Nemilentsau, and G. Hanson, The effects of three-dimensional defects on one-way surface plasmon propagation for photonic topological insulators comprised of continuum media, Sci. Rep. 6, 30055 (2016).

<sup>[4]</sup> A. Okamoto, R. Shindou, and S. Murakami, Berry curvature for coupled waves of magnons and electromagnetic waves, Phys. Rev. B 102, 064419 (2020).

<sup>[5]</sup> S. A. Hassani Gangaraj and F. Monticone, Physical Violations of the Bulk-Edge Correspondence in Topological Electromagnetics, Phys. Rev. Lett. 124, 153901 (2020).

<sup>[6]</sup> S. A. Hassani Gangaraj, G. W. Hanson, M. G. Silveirinha, K. Shastri, M. Antezza, and F. Monticone, Unidirectional and diffractionless surface plasmon polaritons on three-dimensional nonreciprocal plasmonic platforms, Phys. Rev. B 99, 245414 (2019).

<sup>[7]</sup> S. Pakniyat, A. M. Holmes, G. W. Hanson, S. A. H. Gangaraj, M. Antezza, M. G. Silveirinha, S. Jam, and F. Monticone, Nonreciprocal, robust surface plasmon polaritons on gyrotropic interfaces, IEEE Trans. Antenn. Propag. 68, 3718 (2020).

<sup>[8]</sup> S. Pakniyat, Y. Liang, Y. Xiang, C. Cen, J. Chen, and G. W. Hanson, Indium antimonide—constraints on practicality as a magneto-optical platform for topological surface plasmon polaritons, J. Appl. Phys. 128, 183101 (2020).

<sup>[9]</sup> Y. Liang, S. Pakniyat, Y. Xiang, J. Chen, F. Shi, G. W. Hanson, and C. Cen, Tunable unidirectional surface plasmon polaritons at the interface between gyrotropic and isotropic conductors, Optica 8, 952 (2021).

- [10] T. Ochiai, Non-reciprocity and topology in optics: one-way road for light via surface magnon polariton, Sci. Technol. Adv. Mater. 16, 014401 (2015).
- [11] G. W. Hanson, S. A. H. Gangaraj, and A. M. Nemilentsau, Unidirectional, defect-immune, and topologically protected electromagnetic surface waves, in *The World of Applied Electromagnetics: In Appreciation of Magdy Fahmy Iskander*, edited by A. Lakhtakia and C. M. Furse (Springer International Publishing, Cham, 2018), pp. 569–604.
- [12] S. A. H. Gangaraj and G. W. Hanson, Momentum-space topological effects of nonreciprocity, IEEE Antenn. Wirel. Propag. Lett. 17, 1988 (2018).
- [13] K. Shastri, M. I. Abdelrahman, and F. Monticone, Nonreciprocal and topological plasmonics, Photonics 8, 133 (2021).
- [14] F. Monticone, A truly one-way lane for surface plasmon polaritons, Nat. Photon. 14, 461 (2020).
- [15] S. A. H. Gangaraj and G. W. Hanson, Topologically protected unidirectional surface states in biased ferrites: Duality and application to directional couplers, IEEE Antenn. Wirel. Propag. Lett. 16, 449 (2017).
- [16] Y. Hatsugai, Chern Number and Edge States in the Integer Quantum Hall Effect, Phys. Rev. Lett. **71**, 3697 (1993).
- [17] S. A. Skirlo, L. Lu, and M. Soljačić, Multimode One-Way Waveguides of Large Chern Numbers, Phys. Rev. Lett. 113, 113904 (2014).
- [18] W. Gao, M. Lawrence, B. Yang, F. Liu, F. Fang, B. Béri, J. Li, and S. Zhang, Topological Photonic Phase in Chiral Hyperbolic Metamaterials, Phys. Rev. Lett. 114, 037402 (2015).
- [19] F. D. M. Haldane and S. Raghu, Possible Realization of Directional Optical Waveguides in Photonic Crystals with Broken Time-Reversal Symmetry, Phys. Rev. Lett. 100, 013904 (2008).
- [20] S. Raghu and F. D. M. Haldane, Analogs of quantum-Hall-effect edge states in photonic crystals, Phys. Rev. A **78**, 033834 (2008).
- [21] L. Lu, J. Joannopoulos, and M. Soljai, Topological photonics, Nat. Photon. 8, 821 (2014).
- [22] M. G. Silveirinha, Bulk-edge correspondence for topological photonic continua, Phys. Rev. B **94**, 205105 (2016).
- [23] M. G. Silveirinha, Proof of the Bulk-Edge Correspondence through a Link between Topological Photonics and Fluctuation-Electrodynamics, Phys. Rev. X 9, 011037 (2019).
- [24] C. Tauber, P. Delplace, and A. Venaille, Anomalous bulk-edge correspondence in continuous media, Phys. Rev. Res. **2**, 013147 (2020).
- [25] M. Hafezi, E. Demler, M. Lukin, and J. Taylor, Robust optical delay lines via topological protection, Nat. Phys. 7, 907 (2011).
- [26] S. U. Piatrusha, E. S. Tikhonov, Z. D. Kvon, N. N. Mikhailov, S. A. Dvoretsky, and V. S. Khrapai, Topological Protection Brought to Light by the Time-Reversal Symmetry Breaking, Phys. Rev. Lett. 123, 056801 (2019).
- [27] Z. Hayran, A. Hassani Gangaraj, and F. Monticone, Topologically protected broadband rerouting of propagating waves around complex objects, Nanophotonics 8, 1371 (2019).
- [28] S. A. H. Gangaraj and F. Monticone, Topologically protected one-way leaky waves in nonreciprocal plasmonic structures, J. Phys.: Condens. Matter **30**, 104002 (2018).
- [29] R. Camley, Nonreciprocal surface waves, Surf. Sci. Rep. 7, 103 (1987).

- [30] F. Fesharaki, C. Akyel, and K. Wu, Broadband substrate integrated waveguide edge-guided mode isolator, Electron. Lett. 49, 269 (2013).
- [31] F. A. Ghaffar, J. R. Bray, M. Vaseem, L. Roy, and A. Shamim, Theory and design of tunable full-mode and half-mode ferrite waveguide isolators, IEEE Trans. Magn. 55, 1 (2019).
- [32] C. K. Seewald and J. R. Bray, Ferrite-filled antisymmetrically biased rectangular waveguide isolator using magnetostatic surface wave modes, IEEE Trans. Microwave Theory Tech. 58, 1493 (2010).
- [33] K. Fang, Z. Yu, V. Liu, and S. Fan, Ultracompact nonreciprocal optical isolator based on guided resonance in a magneto-optical photonic crystal slab, Opt. Lett. 36, 4254 (2011).
- [34] M. J. Sun, M. W. Muller, and W. S. C. Chang, Thin-film waveguide gyrators: A theoretical analysis, Appl. Opt. 16, 2986 (1977).
- [35] B. R. Vishvakarma and D. Chadha, The surface wave concept in circulator design, Int. J. Electron. 47, 89 (1979).
- [36] S. A. H. Gangaraj and F. Monticone, Coupled topological surface modes in gyrotropic structures: Green's function analysis, IEEE Antenn. Wirel. Propag. Lett. 17, 1993 (2018).
- [37] Z. Wang, Y. Chong, J. Joannopoulos, and M. Soljaci, Observation of unidirectional backscattering-immune topological electromagnetic states, Nature (London) 461, 772 (2009).
- [38] Y. Poo, R.-X. Wu, Z. Lin, Y. Yang, and C. T. Chan, Experimental Realization of Self-Guiding Unidirectional Electromagnetic Edge States, Phys. Rev. Lett. **106**, 093903 (2011).
- [39] W.-J. Chen, S.-J. Jiang, X.-D. Chen, J.-W. Dong, and C. Chan, Experimental realization of photonic topological insulator in a uniaxial metacrystal waveguide, Nat. Commun. 5, 5782 (2014).
- [40] S. A. Skirlo, L. Lu, Y. Igarashi, Q. Yan, J. Joannopoulos, and M. Soljačić, Experimental Observation of Large Chern Numbers in Photonic Crystals, Phys. Rev. Lett. 115, 253901 (2015).
- [41] L. He, Z. Addison, J. Jin, E. Mele, S. Johnson, and B. Zhen, Floquet chern insulators of light, Nat. Commun. 10, 4194 (2019).
- [42] A. Hartstein, E. Burstein, A. A. Maradudin, R. Brewer, and R. F. Wallis, Surface polaritons on semi-infinite gyromagnetic media, J. Phys. C 6, 1266 (1973).
- [43] D. Pozar, *Microwave Engineering*, 4th ed. (Wiley, New York, 2011).
- [44] L. Landau and E. Lifshitz, On the theory of the dispersion of magnetic permeability in ferromagnetic bodies, Phys. Z. Sowjetunion 8, 51 (1992).
- [45] V. V. K. Thalakkatukalathil, Electromagnetic modeling and characterization of anisotropic ferrite materials for microwave Isolators/Circulators, Ph.D. thesis, Université de Bretagne occidentale—Brest (2017), https://tel.archives-ouvertes.fr/tel-01778053.
- [46] H. Y. Yao, W.-C. Chang, L.-W. Chang, and T.-H. Chang, Theoretical and experimental investigation of ferrite-loaded waveguide for ferrimagnetism characterization, Prog. Electromagn. Res. C **90**, 195 (2019).
- [47] T. Gerson and J. Nadan, Surface electromagnetic modes of a ferrite slab, IEEE Trans. Microwave Theory Tech. 22, 757 (1974).
- [48] E. Cojocaru, Modes in dielectric or ferrite gyrotropic slab and circular waveguides, longitudinally magnetized, with open and completely or partially filled wall, J. Opt. Soc. Am. B **27**, 1965 (2010).